Modeling of Tunable Elastic Ultralight Aircraft

Nicholas B. Cramer*
NASA Ames Research Center, Moffett Field, CA 94035

Joseph H. Kim[†]
Stinger Ghaarian Technologies, Inc., Moffett Field, CA 94035

Christine E. Gregg[‡], Kenneth C. Cheung[§], and Sean S. Swei[¶]
NASA Ames Research Center, Moffett Field, CA 94035

Aircraft weight is one of the most critical factors in the design and operation of modern vehicles. The ability to integrate ultra-light materials into the primary load bearing structures has the potential to reduce aircraft weight significantly. Ultralight materials tend to be lattice-based meta-materials that are difficult and computationally expensive to model. One of the advantages of meta-materials is to be able to tune or "program" their bulk material properties through the placement of heterogeneous components in the material. A large amount of time devoted to the simulation in the development time for the tuning of the material can be a barrier to the adoption of large scale lattice materials. In this paper, we present a workflow and analysis tool-set to provide first-order estimates for rapid development of engineered lattice materials for aerospace applications. We present results for estimating the displacement and maximum structural stresses.

I. Nomenclature

$voxel$	=	volumetric pixel
C_l	=	local lift coefficent
c_i	=	local chord at the $i^t h$ node
C_p	=	pressure coefficent
α_T	=	voxel pitch 3 in
θ_{tip}	=	tip twist
U_3	=	vertical displacement
$z_{o_{LE/TE}}$	=	z jig position of the leading/trailing edge at the wing tip
$z_{d_{LE/TE}}$	=	z deformed position of the leading/trailing edge at the wing tip
$x_{o_{LE/TE}}$	=	x jig position of the leading/trailing edge at the wing tip
$x_{d_{LE/TE}}$	=	x deformed position of the leading/trailing edge at the wing tip

II. Introduction

Reducing the of an aircraft is one of the most effective means of increasing its efficiency. This is because the amount of power consumed by an aircraft is roughly proportional to the square of the total vehicle density.[1] There are in general limited opportunities to reduce the aircraft weight through its payload which results in a need to reduce weight through its structural mass. Attempting to reduce structural mass is complicated because of the general relationship between material stiffness, strength, and density. This relationship motivates the industries interest in engineered and lattice materials that demonstrate low relative density at high relative stiffness.[2, 3]

Engineered materials have a lot of promise for the aerospace industry beyond their low weight at high relative stiffness

---

*Research Engineer, Intelligent Systems Division, NASA Ames Research Center
[†]Computer Scientist, Intelligent Systems Division, NASA Ames Research Center
[‡]Research Engineer, Applied Manufacturing Division
[§]Research Scientist, Intelligent Systems Division
[¶]Senior Research Scientist, Intelligent Systems Division

they also have the ability for their bulk material properties to be tuned or "programmed by introducing heterogeneity into the lattice. These heterogeneities often take the form of alteration in the geometry of the unit cell to produce behaviors like coupled mechanical twist[4] or more generic shape and stiffness relationships.[5, 6] This work uses a similar principle, but instead of applying the geometric heterogeneity we apply material heterogeneity to a consistent unit cell geometry.

The ability to tune the aeroelastic response is any extremely attractive application. There have been many attempts to do this in different ways; some of them are actively using traditional flaps and ailerons to shape the wing in flight to reduce wing deflection and drag[7] or gust load alleviation[8]. While active means of shaping the wing in response to the conditions are more flexible passive mechanisms, have a lower energy cost. One of the more common examples is tow-steering. Tow-steering is where the carbon fiber composites have their fibers in an optimal oriented to elicit the appropriate wing shaping at the operational conditions.[9] The proposed tuning using different material voxels is a very similar concept where the polymer matrix for the tow-steering is the predominant voxel material type and the fibers as the less prevalent type of voxel.

While engineered materials have many attractive properties to date, three-dimensional lattice meta-materials have not been effectively manufactured at large scales. [10] The development of manufacturing techniques of cellular materials using discrete building blocks have shown promise as a means of overcoming the traditional manufacturing hurdles associated with this class of materials. In previous works Chueng et. al.[11] demonstrated the ability to construct cellular composite solids from discretely assembled components. This methodology was expanded using planar custom cut airfoil shapes to be applied to a mesoscale active twist aircraft.[12] This method displayed promising applications but is still fundamentally limited to the size of the components that can be cut.

To address the scalability issue associated with a single unit airfoil shape we designed unit cell building block, a voxel (volumetric pixel), shown in Figure 1A as a fundamental building block to construct a larger aircraft. This fundamental building block was used to construct a 14-foot wingspan vehicle.[13] The vehicle was named MADCAT v1 for the project Mission Adaptive Digital Composite Aerostructure Technologies it can be seen in Figure 1 C. One of the goals of this project was to demonstrate the ability to use a high-performance building block to design and test a new aircraft design rapidly. This presents a new paradigm in aerostructure design, where typically the desired geometry is determined, and then the structural aerocoupled analysis is done in an iterative loop. The use of the building block constrains the problem and removes the steps following the development of the outer mold line because by the time the outer mold line is completed the underlying substructure has been designed as well.

To enable this new design approach their needs to be a rapid and efficient means for doing the structural analysis to check the safety factor. This paper develops the methodology and simulation examples for the voxel building block approach. Section III gives a brief overview of the aeroestructure design, Section IV presents the modeling approach, Section V presents the simulation results, and we end with a conclusion.

III. Aerostructure Design

The structural design is based on a fling wing blended body wing (BWB) design. We believe this is an excellent application to apply the voxel building block approach because BWB's have been theorized to be a more efficient design [14] but they would require a complete re-tooling of traditional aircraft manufacturing techniques in order to meet full production. The structure is faceted with all the components being either flat of having a slope of 1/3. This makes it difficult to model but allows for the manufacturing and interface design to be relatively simple.

Figure 1 shows the aerostructure and Table 1 shows the amount of and type of voxel building blocks in each half span of wing. Table 2 has the list of different types of interface structures that were usted to interface with the skin and mounting plates.

Table 1   Summary of building blocks used per half span

Part type	Quantity	Material
1. Ultem 2000 (homogeneous wing)	2088	PEI, 20 % chopped fiber
1a. Ultem 2000 (heterogeneous wing)	1741	PEI, 20 % chopped fiber
2. Ultem 1000 (heterogeneous wing)	347	PEI

Table 2   Summary of interface building blocks used per half span

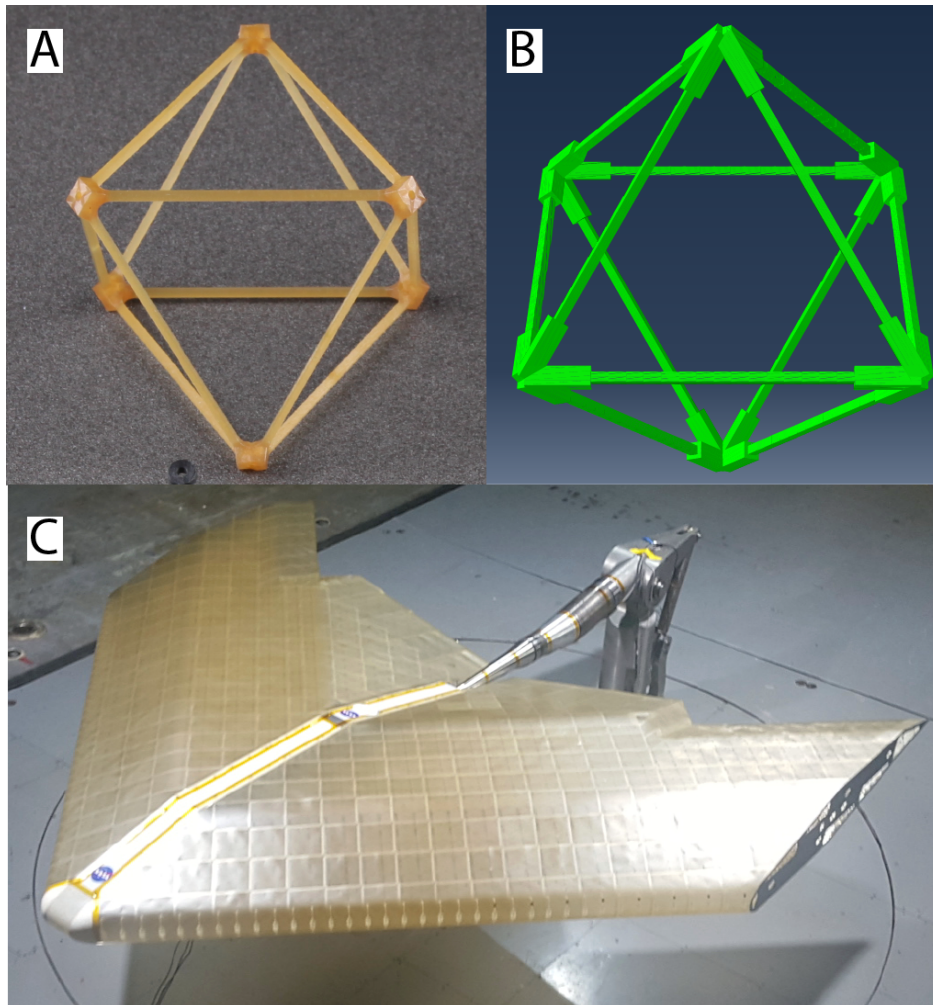| Part type	Quantity	Material
1. Flat interface	414	RTP
2. Slope interface	963	RTP
2a. Slope straight spacer	318	RTP
2b. Slope elbow spacer	309	RTP
3. Leading edge	35	Delrin, 3D print
4. Transition	2	Delrin, 3D print
5. Plate mounting	506	RTP

Fig. 1   A) Cubic octehdral voxel used as the basic building block for the vehicle in C, B) beam based representation of the voxel in A, C) voxel-based prototype

IV. Modeling Approach

The proposed lattice structures that are being used for the substructure have been shown to be ultra-light [13] and previous works have shown that these class of materials inhabit a region of material stiffness that is typically associated with elastomer [15]. The combination of its ultra-light nature and low stiffness means that when it is used to design

an aircraft it inherently becomes a flexible aeroelastic system and requires multiple integration modeling techniques. Figure 2 shows an flow chart of the general approach to the problem.
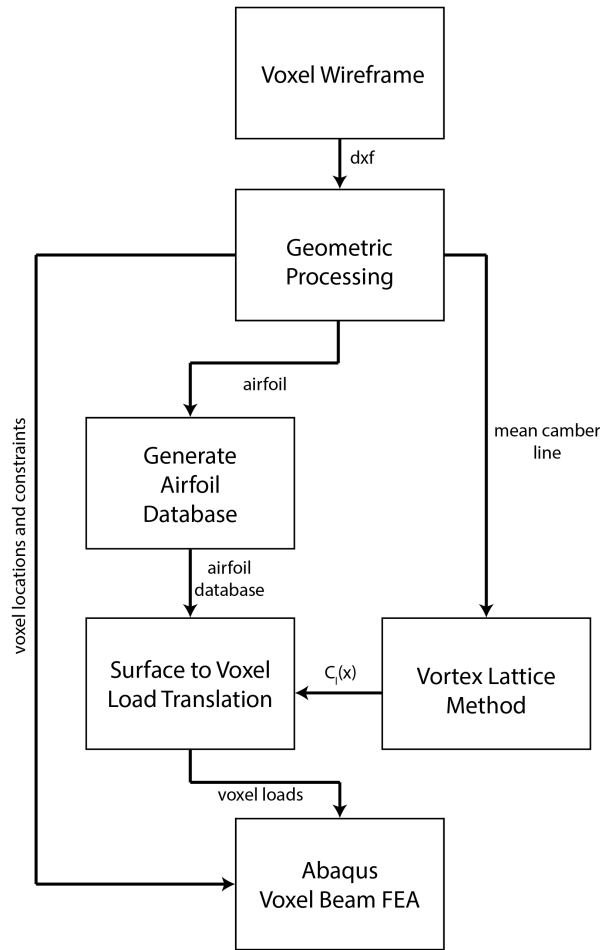
```
                    ┌──────────────────┐
                    │  Voxel Wireframe  │
                    └──────────────────┘
                            │ dxf
                            ▼
                    ┌──────────────────┐
                    │    Geometric      │
                    │   Processing      │
                    └──────────────────┘
              airfoil │           │ mean camber
                      ▼           │    line
            ┌──────────────┐      │
            │   Generate    │      │
            │    Airfoil    │      │
            │   Database    │      │
            └──────────────┘      │
              airfoil │            ▼
             database │    ┌──────────────┐
                      ▼    │ Vortex Lattice│
        ┌──────────────┐   │   Method      │
        │ Surface to Voxel│◄─┤              │
        │ Load Translation│ Cₗ(x)└─────────┘
        └──────────────┘
          voxel loads │
                      ▼
            ┌──────────────┐
            │   Abaqus      │
            │ Voxel Beam FEA│
            └──────────────┘
```

voxel locations and constraints

Fig. 2   Voxel-based airfoil modeling workflow.

In Figure 2, the proposed modeling approach is inherently coupled to the design and production that are a result of the reversible lattice structure. This means that the first output from the designers is a wireframe CAD model and the identification of the basic voxel building block, which in this study is a cubic octohedron. The wireframe is then processed to produce the airfoil sections and the mean camber line which are input to the airfoil database generation and the vortex lattice method (VLM) application, respectively. The VLM provides the spanwise lifting to be used in combination with the airfoil database to generate the voxel loading which is applied in combination with the constrained voxel nodes to an Abaqus beam model which produces the expected deformation of the structure.

The Abaqus beam model that is used can be seen in Figure 1 B where each voxel node was represented by four thicker beams merging into a single node and the voxel struts were broken down into four sub-beams. The beam model voxel ends up with 72 elements and 66 nodes compared to a 3D tetrahedral meshed voxel having 6019 elements and 12217 nodes, nearly two orders of magnitude more elements and three orders of magnitude more nodes. The final version of MADCAT v1 had a total of 2088 voxels which would be $1.2567672e^7$ elements and $2.5509096e^7$ nodes which far exceed the memory limits for Abaqus before the inclusion of the skin and skin support pieces. The validity of this method for cubes of voxels was shown through Instron testing [10], and for this wing with a whiffletree test. [13, 16]

This approach is similar to the approach used by Nguyen et. al.[17] though the low wind speeds do not require any viscous corrections and the early design phase focus of the process allows for a single iteration instead of full convergence. The sacrifice inaccuracy was a design choice that allowed us to iterate and analyze the testing regime of

more than half a dozen designs in a few days.

A. Geometric Processing

The geometric processing is a critical component that is unique to the reversible lattice structure because the design phase builds up the substructure first using basic building blocks. The first rendition of the wing design does not have a clear outer mold line. Instead, it provides wireframes and voxel locations. Figure 3 shows the process for which the necessary outputs for each modeling component must go through. First, an individual cross-section that is based on the size of the voxel is taken to form the wing, and the external boundary points are used to generate an airfoil geometry. Then, that airfoil geometry is used to find the mean camber line using the Voronoi technique [18].
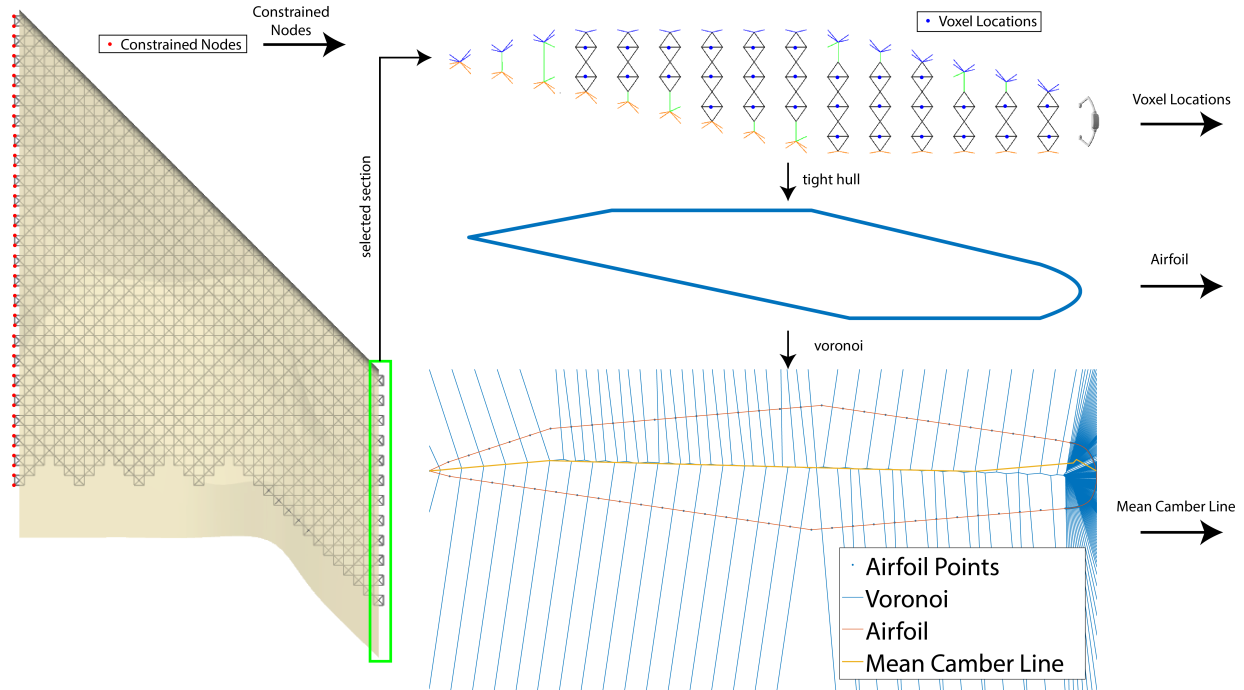
Fig. 3   Flow diagram for voxel-based air vehicle modeling process.

A Voronoi diagram divides the space up around a given set of points so that anything within the area that contains the point is the closest to that point. When applied to an airfoil, the intersection of all of these areas in the center forms the mean camber line with some additional processing. In Algorithm 1 we present the proposed method for using the Voronoi technique and getting the mean camber line. To do this, we first remove any Voronoi points outside of the airfoil because they are not of interest. Then, we define a window and find the range of the airfoil top and bottom for that window to define the maximum thickness in the window. After that, we know the mean camber points must be ones within a given tolerance, which is dependent on the window size and half of the thickness. This produces the mean camber line that is then used for the vortex lattice method.

B. Airfoil Database Generation

The airfoil database was generated using a Matlab wrapper on xFoil [19]. Once the geometric process determined the airfoil geometry, it was filtered five times, then an alpha sweep for each airfoil was completed. The pressure coefficients were then translated into point loads on the boundary hull of the airfoil shape. These boundary point loads were then translated to the underlying voxel substructure by applying their loads to their nearest voxel node; this process is shown in Fig. 4 on the tip airfoil. The k-nearest neighbor approach is not an entirely correct solution to the mapping of the surface loads to the substructure, but the airfoils as an independent subsection are statically in-determinant and not solvable. Furthermore, the skin of the aircraft is segmented to allow the substructure to flex, so that the loads are only translated to the skin support structures directly under the skin, making the nearest neighbor approach a reasonable

Algorithm 1 Geometric Processing

```
 1: procedure GEOMETRIC PROCESSING
 2:     zero airfoil points
 3:     k ← boundary of airfoil points
 4:     v ← voronoin of k
 5:     j ← v internal of k
 6:     window ← chord/window size
 7: loop:
 8:     if max(current window)) < chord then
 9:         window thickness ← max(k(window))-min(k(window)))
10:         dmax ← abs(max(k(window))-j(window)))
11:         dmin ← abs(min(k(window))-j(window)))
12:         camber(i) ← j (abs ( dmax/window thickness − dmin/window thickness ) < tolerance)
13:         i ← i + 1
14:         current window ← window * i
15:         goto loop.
```

approximation.
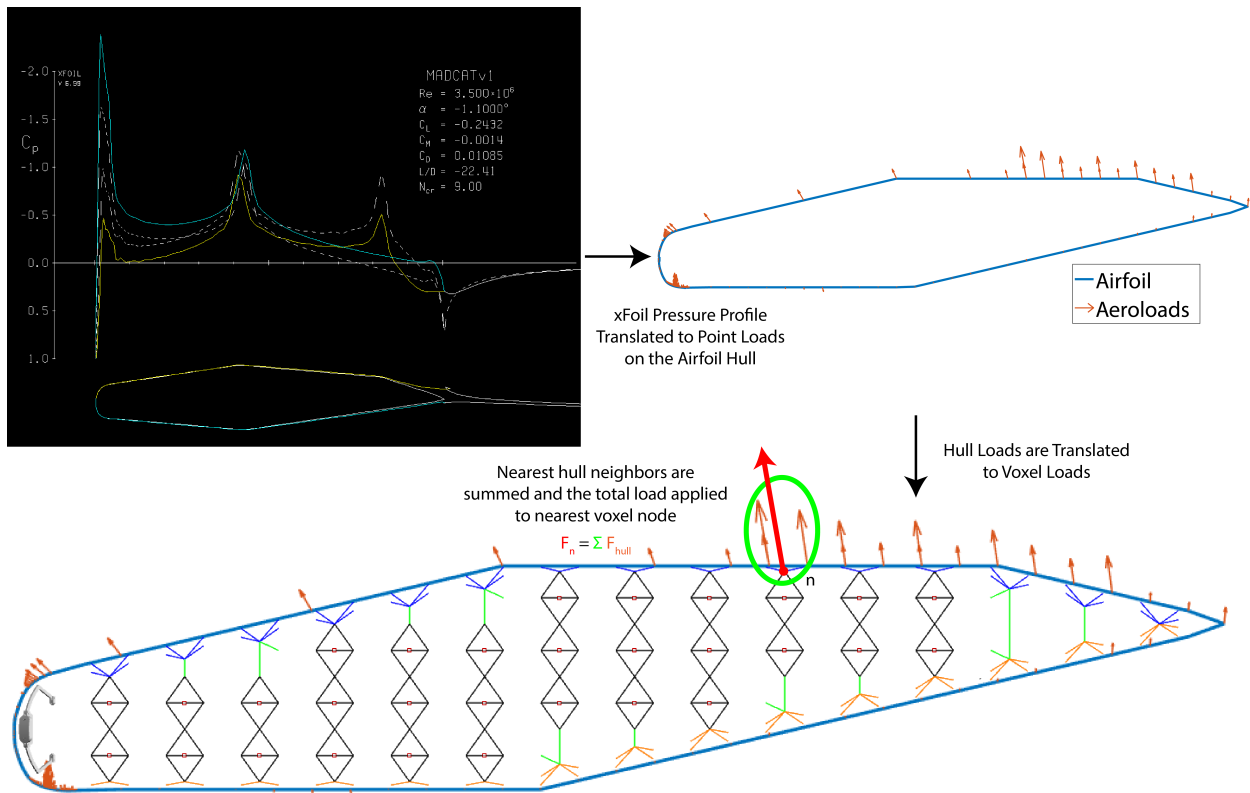
Fig. 4   Boundary point loads on airfoil.

C. Vortex Lattice Method Implementation

The vortex lattice method was used to generate the spanwise loading conditions for the aircraft. This is especially necessary because of the low aspect ratio of the aircraft and significant wing twist. A Matlab version of VLM, Dynamic Tornado, was used, which has been used for modeling of previous ultra-light modular lattice structures [20]. Figure 5 A)

shows the pressure distribution of the aircraft at an angle of attack of 10° and the translation of those pressure to local lift coefficients in Fig. 5. It is worth noting that the center-body of the aircraft is removed from Fig. 5, in order to better visualize the spanwise lift distribution.

From Fig. 5 A) we can see that the pressure distribution has a very high region of pressure located in the inboard sections at the trailing edge that might be numerically sensitive, resulting in the sharp points in Fig. 5 B).

$$C_l = \frac{\sum_{j=1}^{n} C_p(x_i, y_j)}{c_i}$$
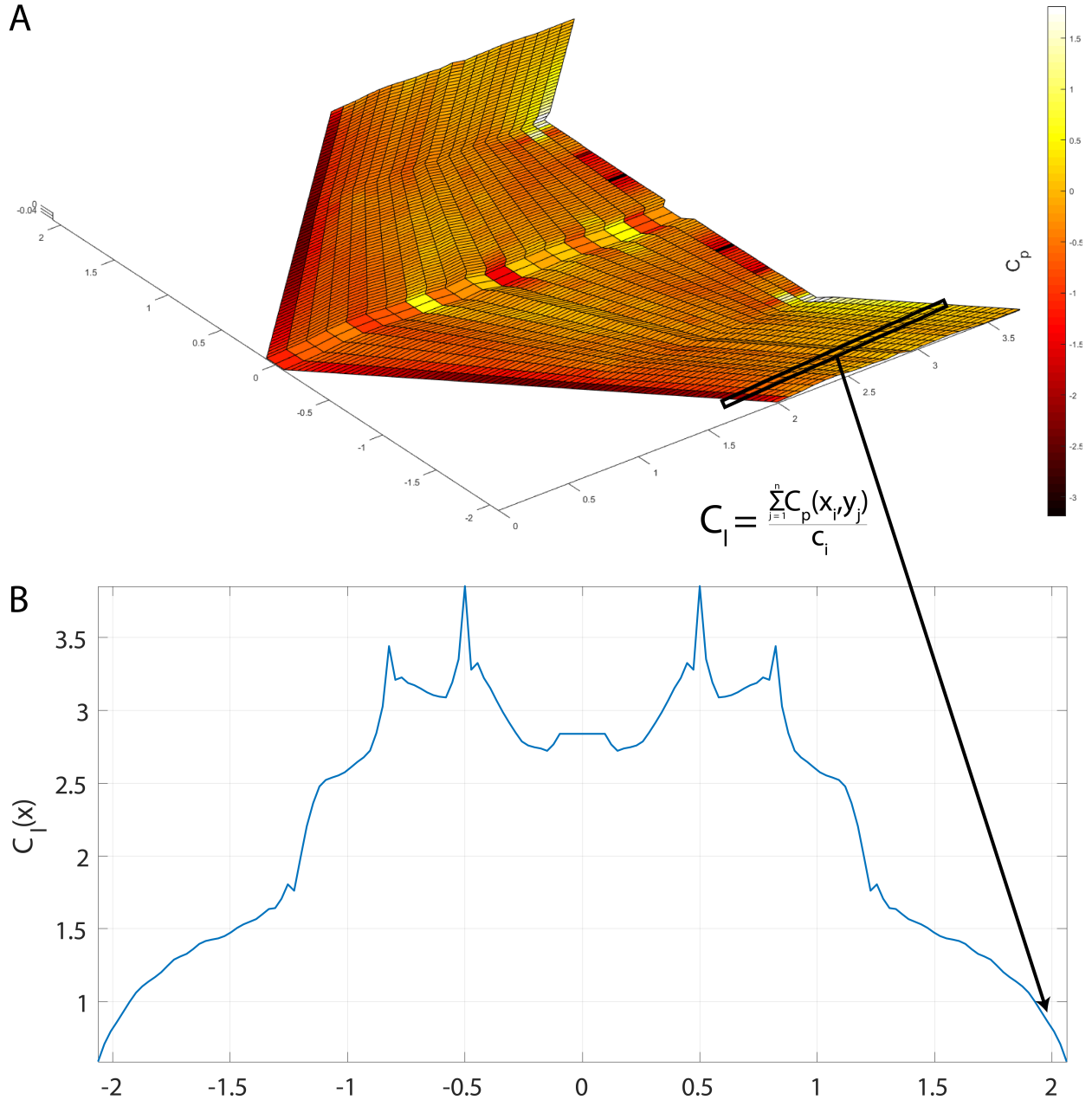
Fig. 5   A) Pressure distribution on blended-wing-body; B) Region of high pressure near trailing edge.

D. Structural Integration

The final component of the modeling is the structural integration that takes in the constraints from the geometric processing and the combined voxel node loads from the VLM and the airfoil database. The substructure is Euler-Bernoulli beams formed into the voxels with subdivisions as shown in Fig. 1 B).

7

1. Aerodynamic Loading

The application of the aero loads to the voxels are taken from the voxel loads in the surface to voxel load translation sub-block. The VLM is used to determine what angle of attack the voxel airfoil load relates to the local lift coefficient and then the loads are applied to the structure. Figure 6 shows the aero loading being applied to the Abaqus structure.
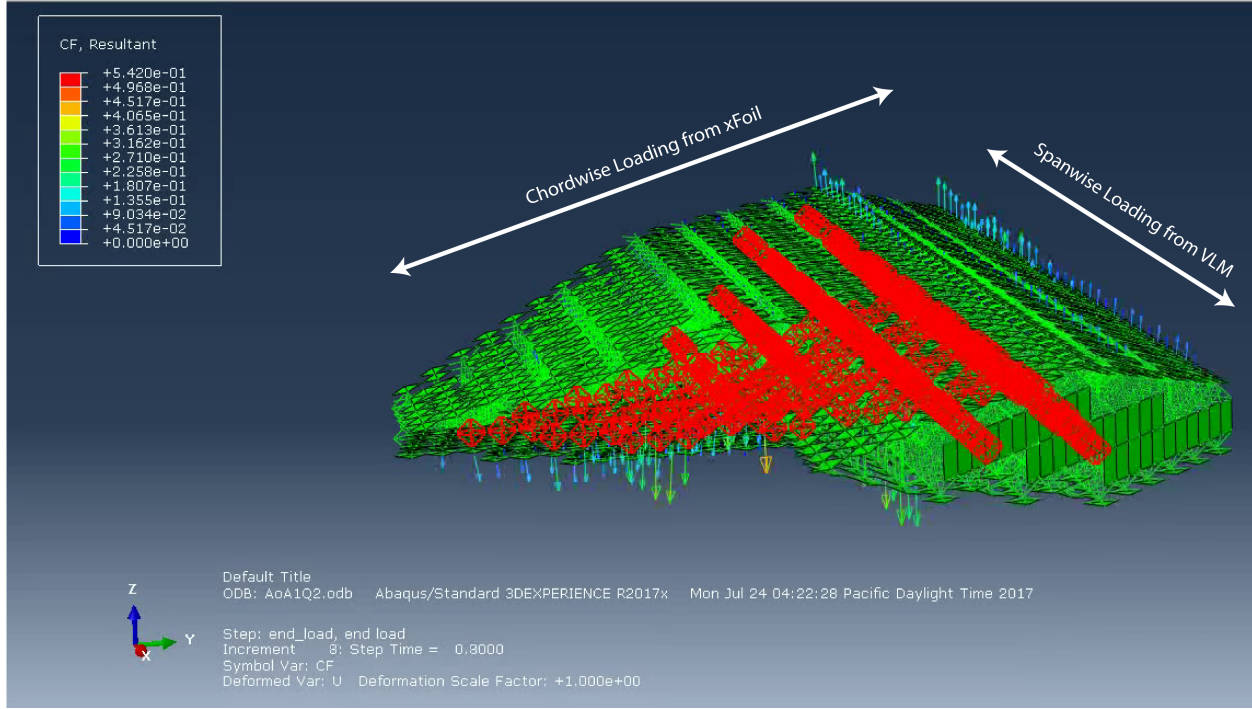

Fig. 6   Aero loading on blended-wing-body aerostructure.

2. Residual Stress

The aircraft substructure can be assembled to tune the bulk material properties by changing the material property of (some) voxels in strategic locations. If the same injection mold is to be used to produce the voxels of different material, then the differences in coefficient of thermal expansion will result in slight different sized voxels. If these voxels of different materials are to be used in the same structure, the assembly process will result in residual stress. To model the residual stress, we use the same procedure presented in Jenett et al. [12]. By applying a negative thermal coefficient of the smaller voxel and then giving the nominal voxels thermal coefficient is set to 0, therefore when the temperature is applied, it would cause the voxels to shrink, simulating the effects of residual stress in the system. This thermal coefficient α_T can be estimated by assessing the change in voxel pitch Δ_p of two different materials, that is

$$\alpha_T = \frac{p^{\frac{\Delta_p}{2}} \frac{\sqrt{2}}{2}}{4} \tag{1}$$

where p is the pitch. In this analysis, we used Ultem 2200 and 1000, which resulted in a Δ_p of 0.01 and hence $\alpha_T = -0.003536$. The residual stress on the structure is shown in Fig. 7 where the stress values are in psi.
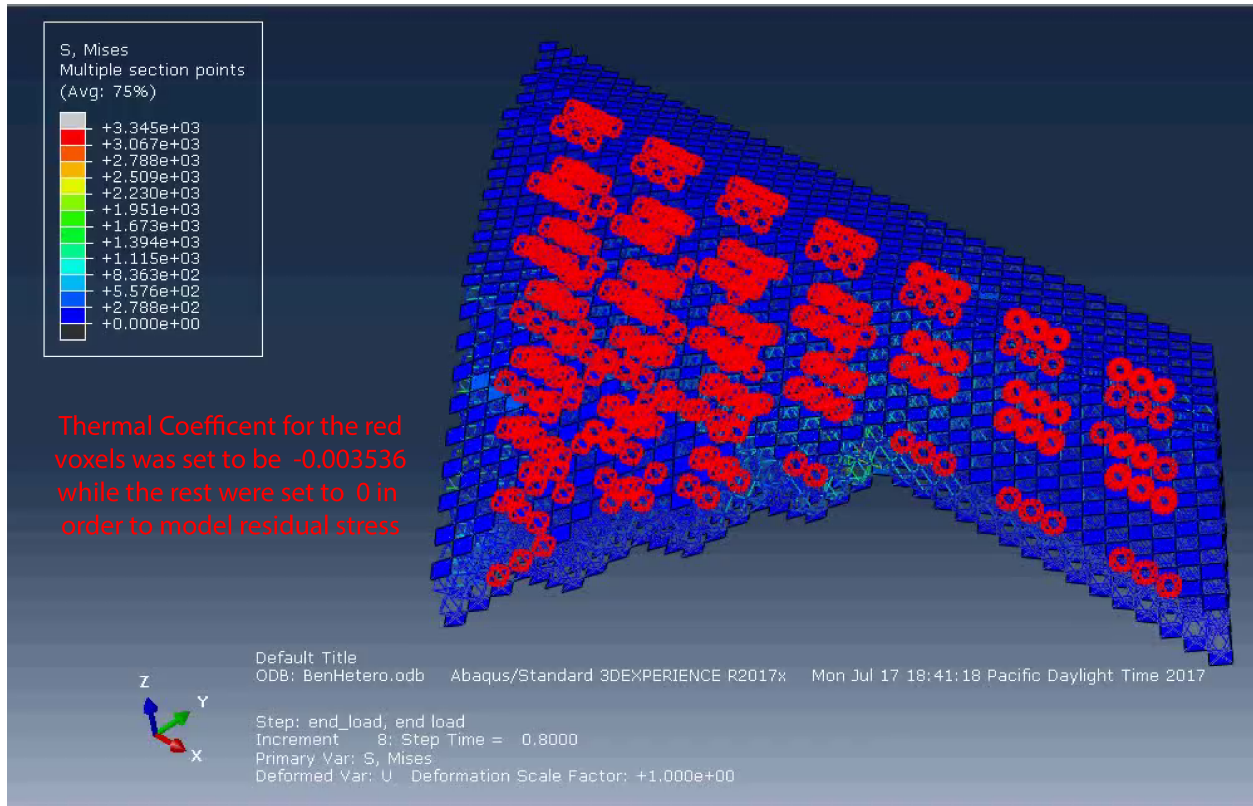
Fig. 7   Deformation and stress resulting from the residual stress due to assembly.

V. Results

Using the simulation methodology outlined above, we simulated the aerostructure and created estimates for the structural safety factor to make testing decisions. The first step was to use the vortex lattice method to simulate the vehicle lift. Figure 8 shows the lift coefficient predicted by the vortex lattice method.
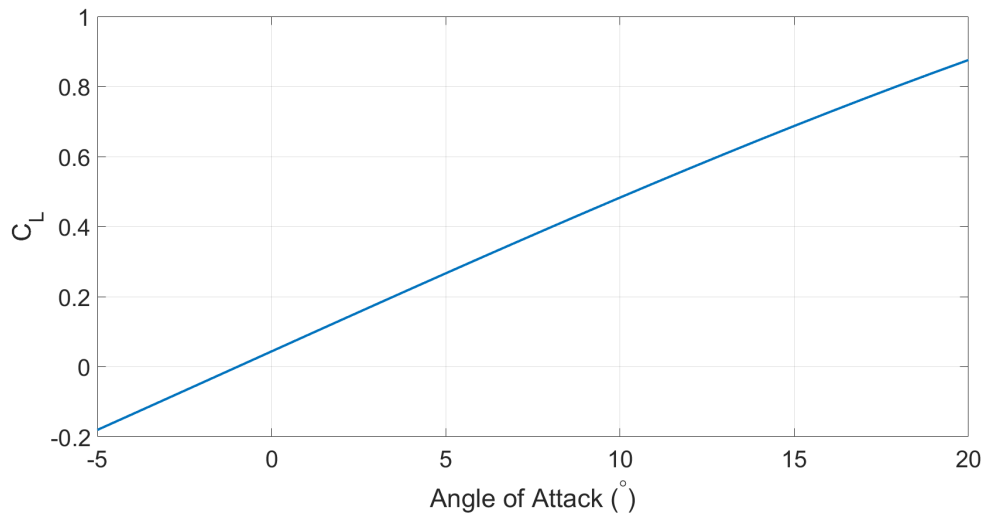

Fig. 8   Lift coefficient with respect to angle of attack from the VLM.

9

The simulations resulted in estimates of the tip twist and tip displacement, shown in Figures 10 and 9 respectively. The tip twist was calculated using Equation 2

$$\theta_{tip} = atan\left(\frac{z_{o_{LE}} - z_{o_{TE}}}{z_{o_{LE}} - x_{o_{TE}}}\right) - atan\left(\frac{z_{d_{LE}} - z_{d_{TE}}}{z_{d_{LE}} - x_{d_{TE}}}\right) \tag{2}$$

where $z_{o/d_{LE/TE}}$ is the vertical jig position or final displaced simulation position of the trailing edge or leading edge and $x_{o/d_{LE/TE}}$ is the horizontal jig position or final displaced simulation position of the trailing edge or leading edge.
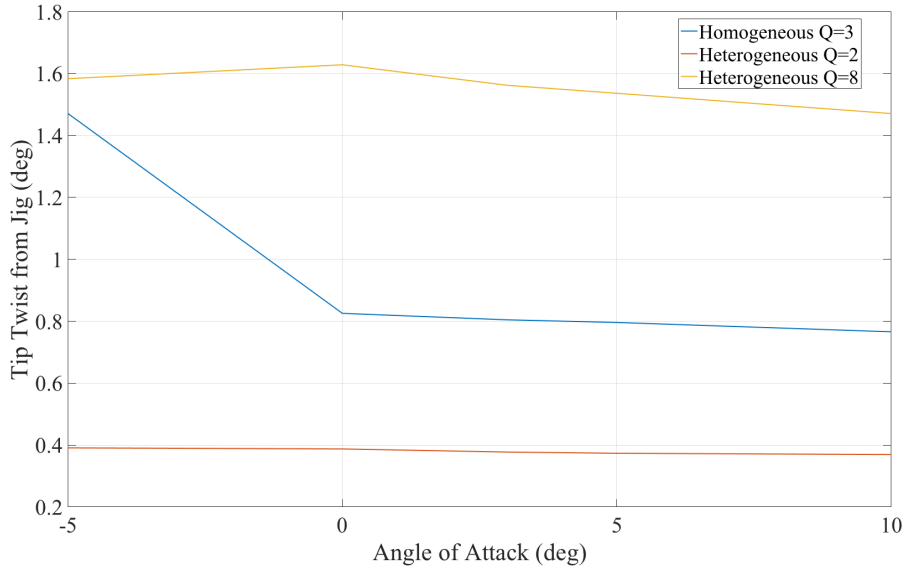

Fig. 9   Simulated tip deflection of the homogeneous and heterogeneous configurations at different dynamic pressures with respect to angle of attack
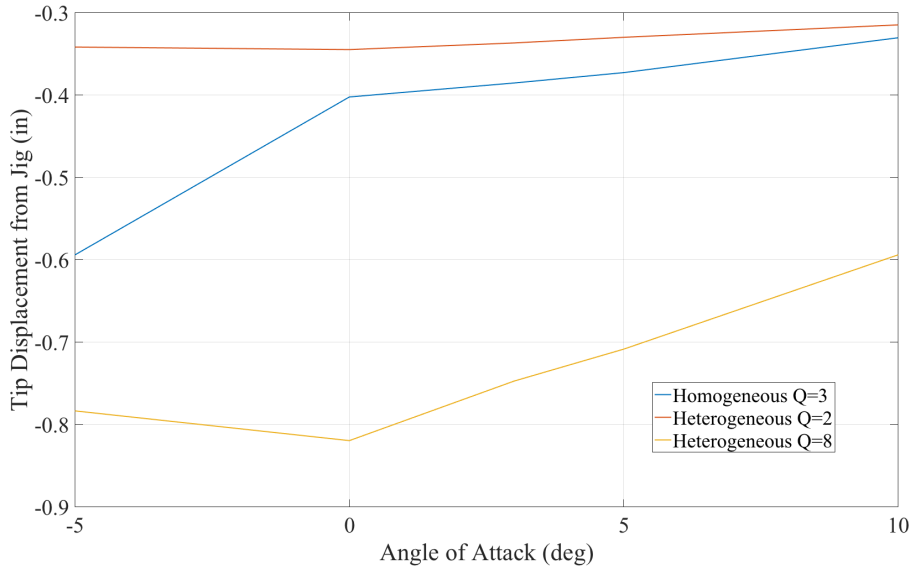

Fig. 10   Simulated tip twist of the homogeneous and heterogeneous configurations at different dynamic pressures with respect to angle of attack

The results from Figure 10 seem a little odd because the tip displacement is always negative even when we have a positive lift. Some of this is the contribution due to gravity, with just gravity applied the homogeneous design had a tip displacement of $-0.148in$, and the heterogeneous had a tip deflection of $-0.219in$, but this does not explain the fact that all of the values even at higher angle of attacks are negative. One explanation of this is that the wing is that the negative forces on the trailing edge shown in Figure 6 have a longer effective moment arm than the ones on the leading edge resulting in an overall negative displacement. Another unexpected result is that the tip displacement of the heterogeneous at a dynamic pressure of 2 psf is less than at 8 psf and the homogeneous at a dynamic pressure of 3 psf. It is a little difficult to compare them because of the difference in dynamic pressures, but they were selected for the reason that will be enumerated below in the stress and safety factor analysis. In this case, the most likely reason for the variation is that the trailing edge downward force had a significant effect on the bending moment than the change from homogeneous to heterogeneous designs.

Angle of Attack (deg)	Max Stress (psi)	Max Strain	Break Safety Factor	Buckle Safety Factor
-5	13890	0.006246	1.76	0.54
0	14800	0.008301	1.37	0.41
3	13120	0.007374	1.55	0.46
5	12250	0.006846	1.65	0.50
10	11530	0.006246	1.76	0.54

Table 3   Heterogenous design maximum stress, strain and associated safety factors at a dynamic pressure of 8 PSF

The primary goal of this analysis was to assess the ultralight building block designs quickly. This was done by looking at the maximum stress, which always occurred at the root, and the maximum strain. The strain was selected as a value of interested because of the lattice beam structures which allow for beam buckling before material failure. We determined that for the voxels, regardless of the material, the maximum strain before buckling was 0.0034 and the material tensile stress at break is 20305.3 psi. Using these values, we first inspected the desired operating condition of a dynamic pressure of 8 psf and focused on the heterogeneous design because of the residual stress all ready acting on the structure. Table 3 shows that we had a material safety factor between 1.37 and 1.76, these values could potentially be acceptable if low for an actual vehicle but tunnel testing the safety factor is expected to be three. The strain shows that the beams would buckle, resulting in the structure entering a nonlinear or secondarily linear regime. In the tables, good safety factors are colored green, questionable ones are colored, orange, and failed safety factors are colored red.

Angle of Attack (deg)	Max Stress (psi)	Max Strain	Break Safety Factor	Buckle Safety Factor
-5	5843	0.001983	3.47	1.72
0	5910	0.002018	3.44	1.68
3	5745	0.001934	3.53	1.76
5	5626	0.00187	3.61	1.82
10	5360	0.001731	3.79	1.96

Table 4   Heterogenous design maximum stress, strain and associated safety factors at a dynamic pressure of 2 PSF

With the close material safety factor and clear, gross buckling occurring in the 8 psf case lowering the dynamic pressure was essential. Due to the residual stress of the heterogeneous system, it was not able to get a meaningful safety factor for the buckling until the dynamic pressure was reduced to 2 psf, the safety factors for which are in Table 4. While beam buckling is not strictly a failure as long as it remains in the elastic regime, it can enter bi-stable conditions that need more analysis to appreciate and for now as avoided.

Angle of Attack (deg)	Max Stress (psi)	Max Strain	Break Safety Factor	Buckle Safety Factor
-5	2563	0.002465	7.92	1.38
0	2620	0.002501	7.75	1.36
3	2555	0.002409	7.95	1.41
5	2537	0.002346	8.00	1.45
10	2475	0.002174	8.20	1.56

Table 5   Homogeneous design maximum stress, strain and associated safety factors at a dynamic pressure of 3 PSF

Following the same selection criteria, a dynamic pressure of 3 psf for the homogeneous design was selected and is shown in Table 5. It is interesting to note that while the dynamic pressure was larger, the maximum stress was lower even though the strain values between the heterogeneous 2 psf and homogeneous 3 psf were similar. Figure 11 shows the maximum stress for the homogeneous wing at 3 psf and the heterogeneous wing at 2 psf. We can see that the maximum stress at an angle of attack of 10° for the homogeneous is actually on the top of the wing root while it is at the bottom of the heterogeneous where we would expect it. Looking closely we can also see that the maximum stress is not on a vertical beam for the homogeneous maximum stress, this combined with the higher amounts of tip twist from Figure 9 suggest that the stress is coming from the torsional motion which could help to explain the amount of strain in Table 5.
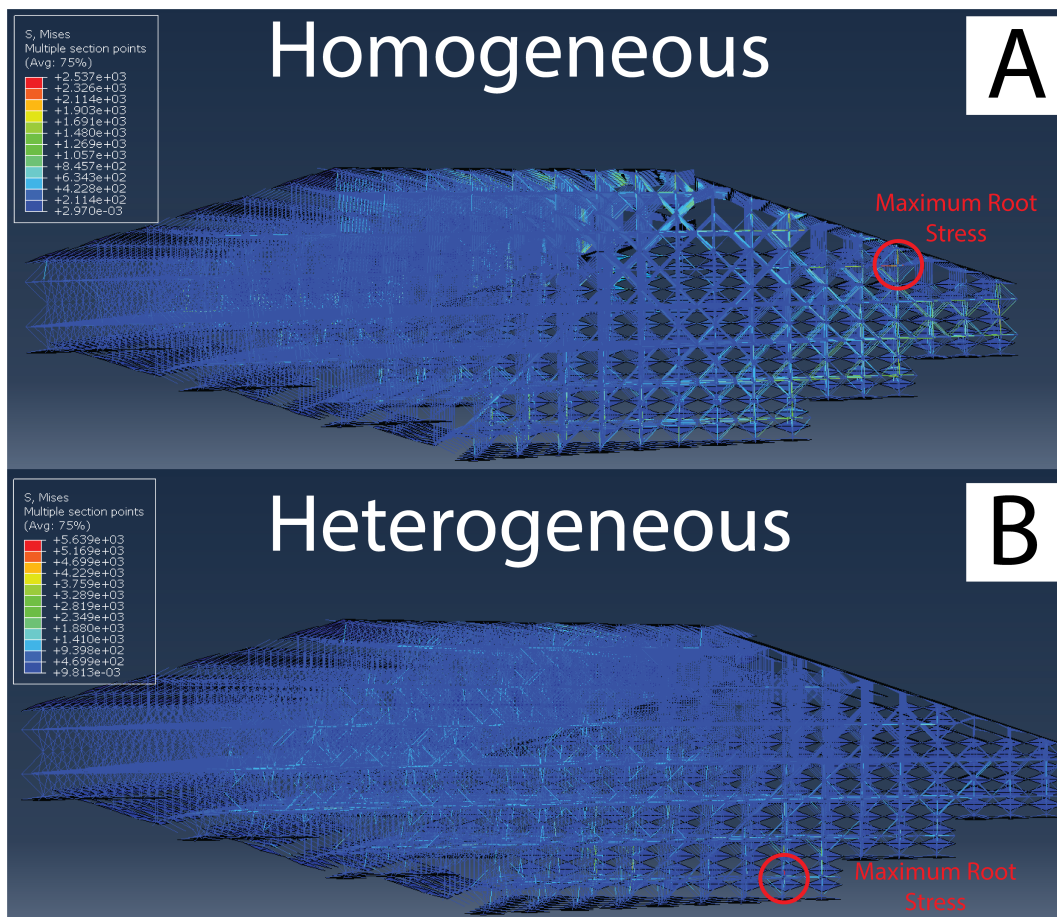

Fig. 11   Comparison the stress distribution at the wing root at an angle of attack of 10° for the homogeneous wing at 3 psf and the heterogeneous wing at 2 psf.

All of the results presented above were simulated with a single iteration not by re-simulating the aeroloading based

on the changes in geometry from the structure. This was done in large part to save on computation time, but some analysis was done by taking the tip twist and displacement and assuming a linear distribution from the root to the tip and then re-calculating the loading. The new aero results were then applied to the Abaqus finite element. We performed this simulation at an angle of attack of 5° and found that all the significant values, tip displacement, tip twist, max stress, and max strain were withing 99.7% justifying the use of a single iteration.

VI. Conclusion

In conclusion, we have presented a methodology and approach to model aerostructures built using discrete voxel unit cells building block based approach. The primary analysis tools were deconstructing the proposed voxel geometry into something usable by a vortex lattice method solver, xFoil, and Abaqus to perform loading simulations. The primary output were the expected safety factors to access the viability of the proposed design. Geometric differences between the voxel pitches resulting in residual stress were addressed using thermal coefficients resulting in a complete model for tunable ultralight aerostructures.

Acknowledgments

References

[1] Bejan, A., *Shape and structure, from engineering to nature*, Cambridge university press, 2000.

[2] Arnold, S. M., Cebon, D., and Ashby, M., "Materials selection for aerospace systems," 2012.

[3] Valdevit, L., Jacobsen, A. J., Greer, J. R., and Carter, W. B., "Protocols for the optimal design of multi-functional cellular structures: from hypersonics to micro-architected materials," *Journal of the American Ceramic Society*, Vol. 94, 2011, pp. s15–s34.

[4] Frenzel, T., Kadic, M., and Wegener, M., "Three-dimensional mechanical metamaterials with a twist," *Science*, Vol. 358, No. 6366, 2017, pp. 1072–1074.

[5] Coulais, C., Teomy, E., de Reus, K., Shokef, Y., and van Hecke, M., "Combinatorial design of textured mechanical metamaterials," *Nature*, Vol. 535, No. 7613, 2016, p. 529.

[6] Florijn, B., Coulais, C., and van Hecke, M., "Programmable mechanical metamaterials," *Physical review letters*, Vol. 113, No. 17, 2014, p. 175503.

[7] Drew, M. C., Hashemi, K. E., Cramer, N. B., and Nguyen, N. T., "Multi-objective Optimal Control of the 6-DoF Aeroservoelastic Common Research Model with Aspect Ratio 13.5 Wing," *AIAA Scitech 2019 Forum*, 2019, p. 0220.

[8] Hashemi, K. E., Nguyen, N. T., Drew, M. C., Chaparro, D., and Ting, E., "Performance Optimizing Gust Load Alleviation Control of Flexible Wing Aircraft," *2018 AIAA Guidance, Navigation, and Control Conference*, 2018, p. 0623.

[9] Stanford, B. K., Jutte, C. V., and Wu, K. C., "Aeroelastic benefits of tow steering for composite plates," *Composite Structures*, Vol. 118, 2014, pp. 416–422.

[10] Gregg, C. E., Kim, J. H., and Cheung, K. C., "Ultra-Light and Scalable Composite Lattice Materials," *Advanced Engineering Materials*, 2018.

[11] Cheung, K. C., and Gershenfeld, N., "Reversibly assembled cellular composite materials," *Science*, 2013, p. 1240889.

[12] Jenett, B., Gregg, C., Cellucci, D., and Cheung, K., "Design of multifunctional hierarchical space structures," *Aerospace Conference, 2017 IEEE*, IEEE, 2017, pp. 1–10.

[13] Cramer, N., Cellucci, D. W., Formoso, O. B., Gregg, C. E., Jenett, B. E., Kim, J. H., Lendraitis, M., Swei, S. S.-m., Trinh, G. T., Trinh, K. V., et al., "Elastic Shape Morphing of Ultralight Structures by Programmable Assembly," *Smart Materials and Structures*, 2019.

[14] Liebeck, R. H., "Design of the blended wing body subsonic transport," *Journal of aircraft*, Vol. 41, No. 1, 2004, pp. 10–25.

[15] Jenett, B., Calisch, S., Cellucci, D., Cramer, N., Gershenfeld, N., Swei, S., and Cheung, K. C., "Digital morphing wing: active wing shaping concept using composite lattice-based cellular structures," *Soft robotics*, Vol. 4, No. 1, 2017, pp. 33–48.

[16] Cramer, N. B., Jenett, B., Swei, S. S.-M., and Cheung, K., "Design Approximation and Proof Test Methods for a Cellular Material Structure," *AIAA Scitech 2019 Forum*, 2019, p. 1861.

[17] Nguyen, N. T., Ting, E., and Chaparro, D., "Development of an Integrated Nonlinear Aeroservoelastic Flight Dynamic Model of the NASA Generic Transport Model," *2018 AIAA/ASCE/AHS/ASC Structures, Structural Dynamics, and Materials Conference*, 2018, p. 2210.

[18] `https://stackoverflow.com/questions/3783207/determining-a-mean-camber-line`, ???? Accessed: 2018-6-11.

[19] Drela, M., "XFOIL: An analysis and design system for low Reynolds number airfoils," *Low Reynolds number aerodynamics*, Springer, 1989, pp. 1–12.

[20] Cramer, N. B., Swei, S. S.-M., Cheung, K., and Teodorescu, M., "Determination of Optimal Wing Twist Pattern for a Composite Digital Wing," *2018 AIAA Information Systems-AIAA Infotech@ Aerospace*, 2018, p. 0892.